JGP Journal of General Physiology

ARTICLE

Pain Focus

Structural basis for severe pain caused by mutations in the voltage sensors of sodium channel $Na_V1.7$

Goragot Wisedchaisri[1], Tamer M. Gamal El-Din[1], Natasha M. Powell[2], Ning Zheng[1,3], and William A. Catterall[1]

Voltage-gated sodium channels in peripheral nerves conduct nociceptive signals from nerve endings to the spinal cord. Mutations in voltage-gated sodium channel $Na_V1.7$ are responsible for a number of severe inherited pain syndromes, including inherited erythromelalgia (IEM). Here, we describe the negative shifts in the voltage dependence of activation in the bacterial sodium channel Na_VAb as a result of the incorporation of four different IEM mutations in the voltage sensor, which recapitulate the gain-of-function effects observed with these mutations in human $Na_V1.7$. Crystal structures of Na_VAb with these IEM mutations revealed that a mutation in the S1 segment of the voltage sensor facilitated the outward movement of S4 gating charges by widening the pathway for gating charge translocation. In contrast, mutations in the S4 segments modified hydrophobic interactions with surrounding amino acid side chains or membrane phospholipids that would enhance the outward movement of the gating charges. These results provide key structural insights into the mechanisms by which these IEM mutations in the voltage sensors can facilitate outward movements of the gating charges in the S4 segment and cause hyperexcitability and severe pain in IEM. Our work gives new insights into IEM pathogenesis at the near-atomic level and provides a molecular model for mutation-specific therapy of this debilitating disease.

Introduction

Voltage-gated sodium (Na_V) channels initiate and propagate action potentials in nerve and muscle. Mutations in the Na_V channel cause hyperexcitability that leads to many diseases, including chronic pain (Dib-Hajj et al., 2013; Mantegazza et al., 2021). Neuropathic pain syndromes are significant health problems that affect millions of people and cost billions of dollars in treatments (Dib-Hajj and Waxman, 2014; Waxman et al., 2014). They arise from damage to peripheral nerves from injury, diabetes, and cancer chemotherapy. However, rare inherited pain syndromes are caused by mutations in the neuronal sodium channel $Na_V1.7$, including inherited erythromelalgia (IEM), paroxysmal extreme pain disorder (PEPD), and small fiber neuropathy (SFN; Dib-Hajj et al., 2013; Dib-Hajj and Waxman, 2019). Patients with these syndromes have episodes of intense pain, redness, and swelling. No targeted treatment for these pain syndromes is available currently, but some patients may respond well to existing pharmacotherapies in selected cases (Geha et al., 2016). On the other hand, homozygous loss-of-function mutations caused by gene truncation or deletion of $Na_V1.7$ produce congenital insensitivity to pain (CIP), a rare disorder in which patients do not feel pain despite having injuries (Cox et al., 2006). As a result, $Na_V1.7$ is an attractive drug target for novel pain treatments that do not involve opioids or lead to addiction (Dib-Hajj and Waxman, 2014).

$Na_V1.7$ is a member of the family of nine human Na_V channel subtypes ($Na_V1.1$–$Na_V1.9$; Catterall, 2000; Ahern et al., 2016; Dib-Hajj and Waxman, 2019). Na_V channels contain 24 transmembrane (TM) segments that form four homologous, but not identical, 6-TM domains (domains I–IV). The first four TM segments in each homologous 6-TM domain (S1–S4) form the voltage-sensing module (VS). The VS is connected to the pore module (PM), formed by the S5 and S6 segments and the P loop between them, via the α-helical S4–S5 linker. These four homologous domains come together to form a functional channel with an ion-conducting pore at its center (Payandeh et al., 2011). Depolarization activates Na_V channels via the "sliding-helix" mechanism, in which positively charged Arg or Lys gating charges in the S4 segment move outward toward the

[1]Department of Pharmacology, University of Washington, Seattle, WA, USA; [2]Graduate Program in Neuroscience, University of Washington, Seattle, WA, USA; [3]Howard Hughes Medical Institute, University of Washington, Seattle, WA, USA.

Correspondence to Goragot Wisedchaisri: goragot@uw.edu

This work is part of a special issue on Mapping the Pain Landscape—From Molecules to Medicine.

extracellular side of the membrane upon depolarization (Ahern et al., 2016; Catterall et al., 2017). Outward S4 movement triggers a major conformational change in the S4–S5 linkers on the intracellular side of the membrane and induces the opening of the activation gate of the pore by bending and rotation of the intracellular ends of the S6 segments (Wisedchaisri et al., 2019). $Na_V1.7$ is expressed mainly in peripheral somatic and visceral sensory neurons in dorsal root ganglia and in sympathetic ganglion neurons, where it serves as a threshold channel that sets the gain of nociceptors for the generation of pain signals (Klugbauer et al., 1995; Dib-Hajj et al., 2013). Its slow rate of closed-state inactivation allows smaller and slower depolarizations to activate the channel and thereby enhances responses to small nociceptive stimuli (Cummins et al., 1998; Dib-Hajj et al., 2013). IEM mutations often cluster in domains I and II and shift the voltage dependence of activation to more negative membrane potentials, allowing smaller depolarizations to trigger an action potential that becomes a pain signal (Dib-Hajj et al., 2013). However, the molecular and structural basis for the pathogenic effects of mutations that result in pain phenotypes in patients remains unclear because there is no high-resolution structural information for the $Na_V1.7$ channel in specific functional states.

While the structures of $Na_V1.7$ have been determined by cryo-EM at high resolution (Shen et al., 2019; Huang et al., 2022), progress toward resolving the structure with IEM mutations has been limited by challenges in obtaining sufficient quantity of $Na_V1.7$ protein (Shen et al., 2021), as well as intrinsic mobility of the VS that reduces the level of local resolution achieved by cryo-EM in the VS, where many IEM mutations are located. To overcome these limitations, we introduced IEM mutations into Na_VAb, a bacterial homolog of mammalian Na_V channels, and determined their structures by X-ray crystallography (Payandeh et al., 2011). The structures of Na_VAb and $Na_V1.7$ are similar in their core transmembrane domains (within <3 Å RMSD; Payandeh et al., 2011; Shen et al., 2019; Huang et al., 2022), and key structural elements involved in the activation of human $Na_V1.7$ are exchangeable between them (Payandeh et al., 2011; Ahuja et al., 2015; Xu et al., 2019; Wisedchaisri et al., 2021). This approach has previously uncovered the structural basis for the gain-of-function phenotypes caused by three IEM mutations in the S4–S5 linkers of $Na_V1.7$, which induce the formation of an additional hydrogen bond in the activated state (Wisedchaisri et al., 2023). Here, we used that powerful approach to investigate the structural basis for the pain-inducing effects of IEM mutations in the VS of $Na_V1.7$. Our structures reveal distinct mechanisms through which IEM mutations in the VS alter the gating movements of the S4 segments and thereby provide a structural and physiological basis for the pain-inducing effects of these $Na_V1.7$ channelopathy mutations at the near-atomic level.

Materials and methods

Materials availability

Further information and requests for resources and reagents should be directed to the corresponding author Goragot Wisedchaisri (goragot@uw.edu). All reagents generated in this study are available from the corresponding author with a completed materials transfer agreement.

Microbe strains

E. coli GC10 was cultured at 37°C in LB medium supplemented with 100 µg/ml of ampicillin for plasmid DNA extraction. *E. coli* DH10Bac was cultured at 37°C in LB medium supplemented with 50 µg/ml kanamycin sulfate, 7 µg/ml gentamicin, and 10 µg/ml tetracycline for bacmid production.

Cell culture

Sf9 (*Spodoptera frugiperda*) insect cells were maintained in Grace's Insect Medium and supplemented with 8–10% FBS and penicillin/streptomycin at 27°C and passaged at 80–95% confluence for baculovirus production. Hi5 (*Trichoplusia ni*) insect cells were maintained and infected in Grace's Insect Medium supplemented with 8–10% FBS and glutamine/penicillin/streptomycin at 27°C for electrophysiology and protein expression.

Mutagenesis and baculovirus production of Na_VAb with IEM mutation

The pFastBac-$Na_VAb\Delta28$ plasmid carrying a C-terminal 28-residue truncation (residues 1–239) of Na_VAb gene (Gamal El-Din et al., 2019) was used as a template for site-directed mutagenesis. To generate a desired plasmid of a Na_VAb mutant, overlapping oligonucleotide primers with a codon changed to a specific mutation were synthesized (Integrated DNA Technologies) and used for site-directed mutagenesis PCR with PfuUltra II Fusion HotStart DNA Polymerase (Agilent). The PCR products were treated with DpnI (New England Biolabs) and transformed into *E. coli* GC10 competent cells (Genesee Scientific). Plasmid DNAs were isolated from transformed colonies using the QIAprep Spin Miniprep Kit (Qiagen) according to the manufacturer's protocol and sequenced to confirm the mutation. Plasmids containing $Na_VAb\Delta28$ with the IEM mutation were used to transform *E. coli* DH10Bac competent cells for bacmid production, and baculoviruses were prepared with Sf9 insect cells using the Bac-to-Bac protocol according to the manufacturer (Life Technologies). All baculoviruses were tested for protein expression in Hi5 insect cells and the expression levels were confirmed by Western blot analysis to be consistent for all mutants. The same batches of baculoviruses were used for both electrophysiology and protein purification experiments.

Electrophysiology of Na_VAb with IEM mutations

Hi5 insect cells were infected with baculovirus containing $Na_VAb\Delta28$ with an IEM mutation (Gamal El-Din et al., 2019). After 24–48 h, whole-cell sodium currents were recorded using an Axopatch 200 amplifier (Molecular Devices) with glass micropipettes (1.5–2.5 MΩ; Gamal El-Din et al., 2019). The intracellular pipette solution contained (in mM): 35 NaCl, 105 CsF, 10 EGTA, and 10 HEPES, pH 7.4 (adjusted with CsOH). The extracellular solution contained (in mM): 140 NaCl, 2 $CaCl_2$, 2 $MgCl_2$, and 10 HEPES, pH 7.4 (adjusted with NaOH). Linear capacitance was subtracted and 80–90% of series resistance was compensated using internal amplifier circuitry. Current versus voltage (I/V) relationships of the peak currents were recorded in

response to steps to voltages ranging from −160 to +160 mV in 10-mV increments from a holding potential of −160 or −180 mV. Pulses were generated and currents were recorded using Pulse software controlling an InstruTECH ITC-18 interface (HEKA). Data were analyzed using Igor Pro 8 (WaveMetrics).

Analysis of electrophysiological data

Voltage-clamp data were analyzed using Igor Pro 8 (WaveMetrics). The peak current at each voltage of the current family was plotted as a function of the stimulus voltage to visualize the I/V relationship. Normalized conductance/voltage (G/V) curves were calculated from the I/V curves and fit with a simple one-component Boltzmann equation $1/[1 + \exp(V_a - V_m)/k]$, in which V_m is the stimulus potential, V_a is the half-activation voltage, and k is a slope factor. The half-time (τ) for inactivation was measured from the peak of each current trace. A single exponential function was used to fit the inactivation kinetics of all mutants. The data were presented as the mean and standard error of the mean (SEM). Statistical significance was evaluated with Student's *t* test.

Protein expression and purification of Na_VAb with IEM mutations

Third passage (P3) baculoviruses for $Na_VAb\Delta28$ with an IEM mutation were used to infect Hi5 cells in single-layer culture dishes (~12 dishes for each preparation), and the cells were incubated at 27°C for ~72 h. Cells were harvested by centrifugation, and the pellets were resuspended in Buffer A (50 mM Tris HCl, pH 7.5, and 200 mM NaCl) supplemented with 1 mM PMSF, 2× SigmaFast protease inhibitor cocktails (MilliporeSigma), benzamidine HCl, and DNase I. Cells were lysed by sonication and membranes were solubilized with 1% high-purity digitonin (MilliporeSigma) for 1 h at 4°C with gentle mixing. The mixture was centrifuged at 15,000 × *g* for 30 min at 4°C and the supernatant was incubated with Anti-FLAG-M2 affinity gel (MilliporeSigma) for 1 h at 4°C with gentle mixing. The resins were washed with Buffer B (Buffer A supplemented with 0.12% digitonin) and the bound protein was eluted with Buffer C (Buffer B supplemented with 200 µM FLAG peptide). Eluted protein was concentrated to 1 ml using Vivaspin20 100 kD MWCO (Cytiva) and further purified with Superdex S200 size-exclusion chromatography (Cytiva) using 10 mM Tris HCl, pH 7.5, 100 mM NaCl, and 0.12% digitonin as a column running buffer. Elution fractions were evaluated using SDS-PAGE and peak fractions were combined and concentrated to a final concentration of ~20 mg/ml. Protein concentrations were estimated using 1 A_{280} absorbance unit = 1 mg/ml on a NanoDrop spectrophotometer.

Crystallization of Na_VAb with IEM mutations

Na_VAb-bicelle complexes were prepared by mixing $Na_VAb\Delta28$ with an IEM mutation with 10% bicelle (7.5% wt/vol DMPC and 2.5% wt/vol CHAPSO) at 1:4 or 1:5 vol ratios to obtain final 3.0–3.5 mg/ml protein concentration. The complexes were screened for crystallization conditions under 1.70–1.95 M ammonium sulfate and 0.1 M sodium citrate tribasic, pH 4.6–6.0 (Hampton Research). Crystals were cryo-protected by stepwise transfers to a series of cryo-protectant solutions containing 6–30% glucose (6% increments) with the same concentration of ammonium sulfate and sodium citrate in which the crystals were grown.

X-ray data collection and structure determination of Na_VAb with IEM mutations

Crystals were tested for diffraction and data were collected at Advanced Light Source (ALS) beamlines 5.0.3, 8.2.1, and 8.2.2 (Howard Hughes Medical Institute). Diffraction data were processed using the HKL2000 program (Otwinowski and Minor, 1997) with anisotropic scaling and truncation due to anisotropic diffraction. Structures were solved by molecular replacement with PHASER (McCoy et al., 2007) using the previously determined Na_VAb structure (PDB accession no. 3RVY; Payandeh et al., 2011, or PDB accession no. 6MWA; Gamal El-Din et al., 2019) as a search model and refined with REFMAC (Murshudov et al., 2011) in the CCP4 program suite (Winn et al., 2011). Manual model building and local real space refinement were carried out in COOT (Emsley et al., 2010), followed by structure refinement in REFMAC. Subsequently, structures were refined with Phenix.refine module and the final structures were analyzed and validated using MolProbity in the Phenix program suite (Liebschner et al., 2019; Tables S3).

Modeling of Na_VAb structure with IEM mutations in the resting state

Homology models of Na_VAb tetramer structure with the IEM mutations in the resting state were generated with Modeller 10.2 (Webb and Sali, 2016) using the disulfide-locked Na_VAb/KAV/G94C/Q150C cryo-EM structure (PDB accession no. 6P6W; Wisedchaisri et al., 2019) as a template. Structure figures and morph movies were made with Pymol (Schrodinger).

Online supplemental material

Fig. S1 shows multiple amino acid sequence alignments of Na_VAb and human $Na_V1.7$. Table S1 lists IEM mutations in the VS of $Na_V1.7$ for this study. Table S2 lists the activation properties of Na_VAb and $Na_V1.7$ with the IEM mutations. Table S3 shows X-ray data collection and refinement statistics of the $Na_VAb\Delta28$ structures with the IEM mutations.

Results

Structure and function of Na_VAb with $Na_V1.7$ IEM mutations

We surveyed IEM mutations in human $Na_V1.7$ in the literature and selected several mutations for structural and functional studies. In this report, we focus our analysis on Na_VAb structures with four IEM mutations in the VS of $Na_V1.7$ (Fig. 1) that potentially affect channel activation by modifying the movement of the S4 segment. Their positions in the structures of $Na_V1.7$ and Na_VAb are shown in Fig. 1, A–C, and their genetic background, phenotypic properties, and biophysical effects are described in Tables S1 and S2. We introduced each of these IEM mutations into the C-terminal-truncated construct $Na_VAb\Delta28$, and expressed, purified, and crystallized the mutant Na_VAb proteins as described previously (Wisedchaisri et al., 2023). All of these constructs conduct voltage-gated sodium currents that

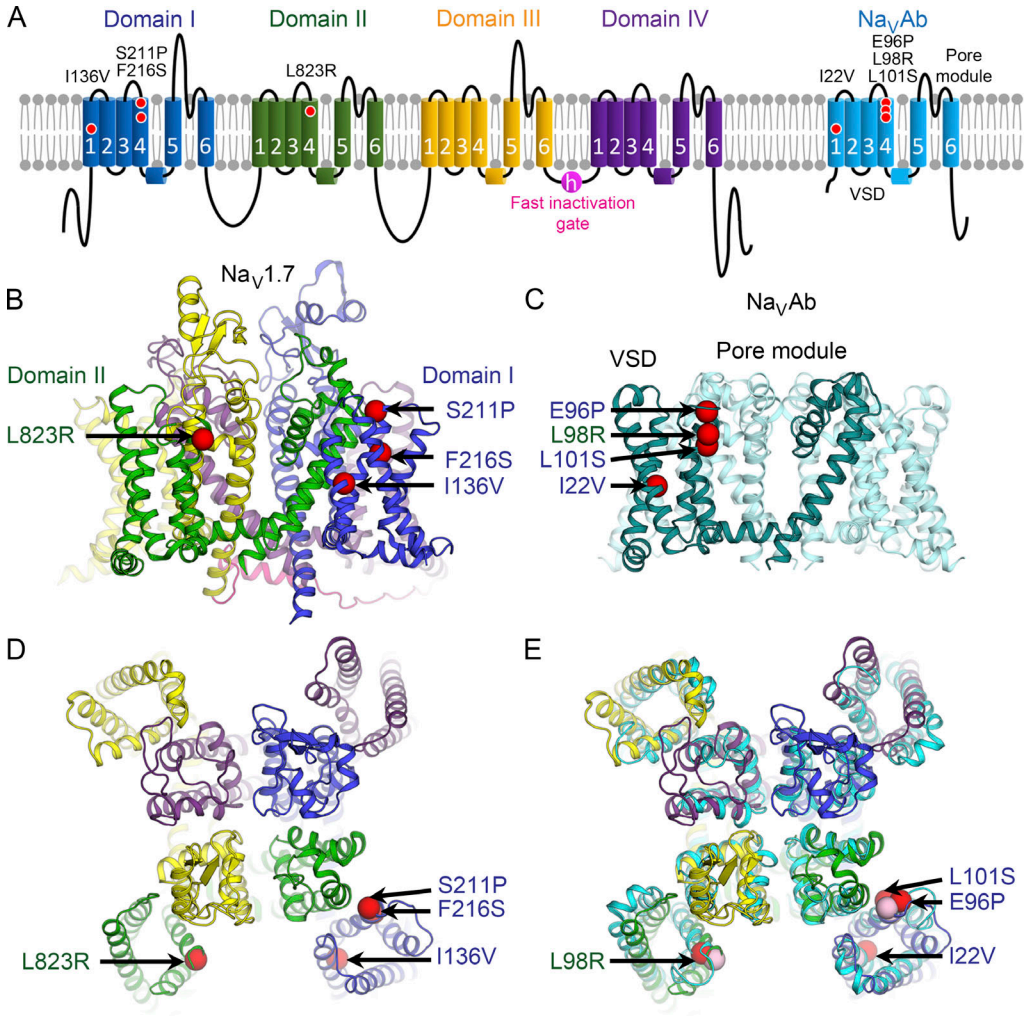

Figure 1. **IEM mutations in voltage sensors of $Na_V1.7$ and Na_VAb. (A)** Topology diagram of $Na_V1.7$ with four IEM mutations (red circles) in the VS of domains I and II selected for this study (left). Equivalent IEM mutations were introduced into the homotetrameric bacterial channel Na_VAb (cyan) for electrophysiological and structural characterization (right). **(B)** Structure of human $Na_V1.7$ with the locations of four IEM mutations mapped onto the model presented in side view (red spheres). Each domain is colored as in A. **(C)** Structure of Na_VAb with the locations of four IEM mutations mapped onto the model presented in side view (red spheres). For clarity, the IEM mutations are shown only in one subunit (teal). Due to the homotetrameric nature of Na_VAb, the mutations are also present in the remaining subunits (cyan). **(D)** Structure of human $Na_V1.7$ with the locations of four IEM mutations mapped onto the model in the top view (red spheres). **(E)** Structure of Na_VAb (cyan) with the locations of four IEM mutations mapped onto the model in the top view (red spheres). For clarity, the IEM mutations are shown only in one subunit. Due to the homotetrameric nature of Na_VAb, the mutations are also present in the remaining subunits. The structure of $Na_V1.7$ from D is superimposed (with the IEM mutations shown as pink spheres).

activate and inactivate rapidly (Fig. 2, A, C, and D), and their voltage dependence of activation (V_a) is negatively shifted to different extents as expected for IEM mutations (Fig. 2 B). All structures were determined for Na_VAb channels embedded in lipid bicelles by X-ray crystallography at a resolution ranging from 2.5 to 3.3 Å, which yielded near atomic clarity in most cases (Table S3). All structures have their VS in the activated state, as determined by the outward position of the S4 segment, while the pore is closed at the activation gate formed by the intracellular ends of the S6 segments. To gain insight into the conformational transitions that are altered by the IEM mutations during activation of the VS, we generated structural models of the Na_VAb IEM mutants in the resting state using the disulfide-crosslinked resting-state structure of Na_VAb as a template (Wisedchaisri et al., 2019). Our results presented below reveal an underlying mechanism for hyperexcitability, by which these IEM mutations modify S4 interactions with nearby amino acid residues and lipids, potentially reducing the energy barrier to outward movement of the gating charges.

Four IEM mutations in the VS

The mutations in the VS are located in the S1 segment in domain I of $Na_V1.7$ (I136V), in the extracellular half of the S4 segment in domain I of $Na_V1.7$ (S211P and F216S), and in the extracellular half of the S4 segment in domain II of $Na_V1.7$ (L823R; Fig. 1, A and B). They are equivalent to Na_VAb I22V, E96P, L101S, and L98R, respectively (Fig. 1 C). Each structure in this group is similar to the $Na_VAb\Delta28$ WT structure (Gamal El-Din et al., 2019) with an overall Cα RMSD of <0.7 Å, indicating minimal alteration of the overall backbone structure by the mutations. When expressed in

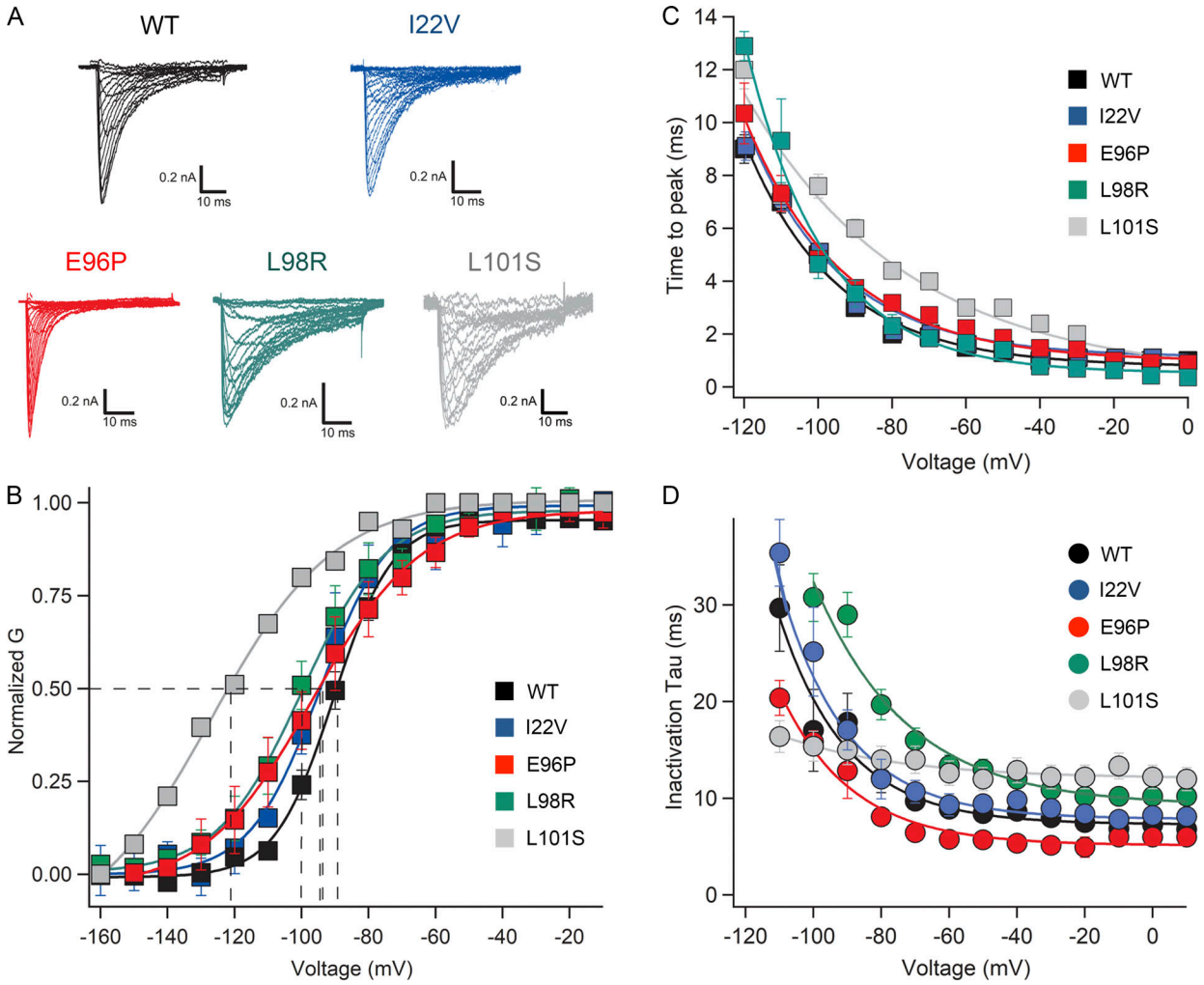

Figure 2. **Functional properties of $Na_VAb\Delta28$ with IEM mutations. (A)** Families of sodium currents for Na_VAb/WT (black), I22V (blue), E96P (red), L98R (green), and L101S (gray). Na_VAb/WT and mutants were expressed in Hi5 insect cells and studied by whole-cell voltage clamp recording as described in Materials and methods. **(B)** Voltage-dependence of activation of Na_VAb/WT and mutants. I/V relationships of the peak sodium currents were recorded in response to steps to voltages ranging from −160 to +20 mV in 10-mV increments from a holding potential of −160 or −180 mV. G/V relationships were calculated as described in Materials and methods. The plots for each mutation are colored as in A. **(C)** Time to reach peak current is plotted as a function of stimulus voltage as calculated from results in A. The plots for each mutation are colored as in A. **(D)** Meantime constants for inactivation calculated from the results of experiments similar to those in A as described in Materials and methods. The plots for each mutation are colored as in A.

Hi5 insect cells, these IEM mutations in the VS cause negative shifts in V_a of Na_VAb from −4 to −29 mV (Fig. 2 B and Table S2).

$Na_V1.7$ I136V/Na_VAb I22V

The Ile residue at this position in the S1 segment is conserved in all domains of Na_V channels and Na_VAb (Fig. S1) and forms part of the hydrophobic constriction site in the VS, along with the conserved Phe residue (F56) in S2, which creates a water-impermeable seal at the center of the VS to focus the electric field (Fig. 3, A and B). The mutation I22V caused a shift of −4 mV in the V_a of Na_VAb (Fig. 2 B and Table S2) comparable with the shifts of −5.7 and −12.2 mV observed for $Na_V1.7$/I136V (Cheng et al., 2008; Wu et al., 2013). In addition, the Na_VAb/I22V mutation did not show any significant change in the kinetics of activation (Fig. 2 C) but caused a slightly slower rate of inactivation (Fig. 2 D). This is similar to the changes in activation and inactivation kinetics observed in $Na_V1.7$/I136V (Cheng et al., 2008; Wu et al., 2013). The structure of Na_VAb/I22V at 2.5-Å resolution reveals a slight local conformational change in the rotamer of the fourth gating charge Arg (R108 or **R4**; Fig. 3, A and B). This small structural change is mostly due to a reduction in the volume of the I22V side chain. In WT, the Ile22 side chain forms a van der Waals contact with the side chain of the gating charge **R4** at the C_β, C_γ, and C_δ positions with its C_δ (Fig. 3 C). Replacement of the side chain of Ile22 by Val (ΔC_δ) creates extra space in the surrounding area and provides the **R4** side chain more flexibility and degrees of freedom of movement. In the resting state (Wisedchaisri et al., 2019), the C_δ atom of Ile22 interacts with the side chains of the second gating charge Arg (R102 or **R2**) and F56. The reduction in the volume of the I22V side chain appears to destabilize the resting state by reducing these van der Waals interactions and also creates more space to allow more flexibility

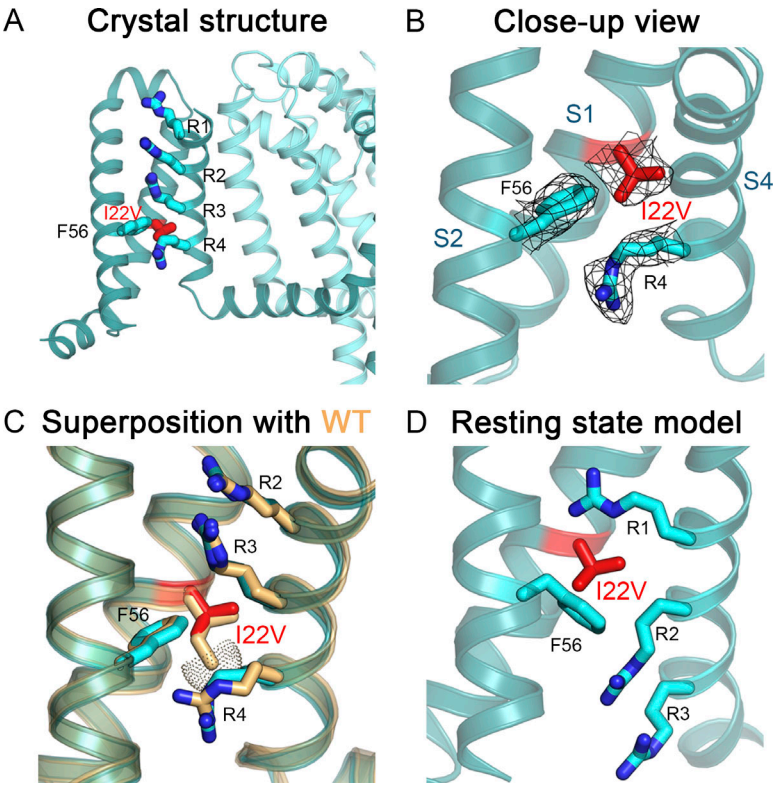

Figure 3. **Structure of Na_VAb/I22V. (A)** Crystal structure of Na_VAb I22V with the mutation shown in red. **(B)** Close-up view of Na_VAb I22V structure in the activated state (teal). Side chains of residues I22V (red), Phe56, and Arg108 (**R4**; cyan) are shown as sticks with the σ_A-weighted $2F_O$-F_C electron density map contoured at 1.0σ level overlaid (mesh). **(C)** Comparison of Na_VAb I22V structure (teal) with the structure of Na_VAb WT (light orange). Side chains of the gating charges **R2** to **R4** are shown as sticks. The I22V mutation lacks the C_δ atom present in Ile22 and results in more space for **R4** to change conformations. The van der Waals hemisphere of Ile22 C_δ is shown as dots. $Na_VAb\Delta28$ (PDB accession no. 6MWA) was used for the comparison as WT. **(D)** Homology model of Na_VAb I22V structure in the resting state.

for the **R2** side chain to move more easily in response to smaller changes in membrane potential (Fig. 3 D). (R# in boldface signifies the consensus numbering of gating charge arginine residues on S4 of voltage-gated ion channels, while R# in regular font shows residue number specific for Na_VAb.)

How does I136V in $Na_V1.7$ cause channel hyperexcitability? During the course of VS activation, the S4 segment moves outward in response to depolarization to activate the VS and trigger pore opening (Wisedchaisri et al., 2019). The trajectory of the S4 segment involves a vertical sliding movement of two helical turns that translocates two gating charges Arg above the hydrophobic constriction site. Since Ile136 is part of the hydrophobic constriction site that interacts with the Arg gating charges in S4 during voltage sensor activation, the I136V mutation likely destabilizes the resting state and reduces the energy barrier for S4 movement by creating more space, thereby making it easier for the S4 segment to activate at more negative membrane potential (Fig. 3 D and Video 1). Because voltage-dependent activation of sodium channels is a nonequilibrium process in which activation races against fast inactivation to activate and open the pore, both destabilization of the resting state and reducing the energy barrier for S4 movement would contribute to the negative shift in V_a. In this way, these structural mechanisms would work together to facilitate the outward movement of S4 and activate $Na_V1.7$-VS1, which is the first domain to move in response to membrane depolarization and set the stage for channel activation during an action potential (Chanda and Bezanilla, 2002).

$Na_V1.7$ S211P/Na_VAb E96P

The Ser residue in this position is conserved in domains I and II of all human Na_V subtypes except $Na_V1.9$. It is located three residues before the first Arg gating charge (R214 or **R1**) at the start of the S4 segment in domain I (Fig. S1). Bacterial Na_V homologs often contain a Ser or a Thr residue in this position (Koishi et al., 2004). However, Na_VAb uniquely contains Glu (E96) at this location. Mutation of this residue to Pro (E96P) causes a −7 mV shift in V_a (Fig. 2 B and Table S2), comparable to the shift of −8.2 mV observed for $Na_V1.7$/S211P (Estacion et al., 2010). We did not observe a significant change in time to peak activation for Na_VAb/E96P (Fig. 2 C). However, the rate of inactivation was significantly faster for the E96P mutant than for the WT (Fig. 2 D). This is consistent with the faster inactivation kinetics for S211P mutation in $Na_V1.7$ (Estacion et al., 2010). When Glu96 of Na_VAb was mutated to a Ser, as in $Na_V1.7$ WT, the V_a of Na_VAb E96S was positively shifted by +20 mV compared with Na_VAb WT (Table S2). Based on these results, the shift in V_a from Ser to Pro at this position (S96P) amounted to a hefty change in V_a of −27 mV (from V_a of −70 mV for E96S to V_a of −97 mV for E96P).

The crystal structure of Na_VAb/E96P shows a local conformational change in the extracellular S3–S4 loop at the start of the S4 segment (Fig. 4, A and B). In the WT structure, the backbone carbonyl oxygen of Glu96 forms a hydrogen bond to the amide nitrogen of Val100 with a distance of 2.8 Å as an α helix (Fig. 4 C). The Glu side chain in WT also stabilizes the first Arg gating charge (**R1**) one helical turn away via charge–charge interaction. However, in the mutant structure, the E96P backbone no longer maintains the hydrogen bond, as the distance between the carbonyl oxygen of E96P and the amide nitrogen of Val100 increases to 4.4 Å (Fig. 4, B and C). Since the S3–S4 linker moves substantially outward during activation of the VS (Wisedchaisri et al., 2019), its looser structure in E96P may favor voltage-dependent activation. In addition to this structural

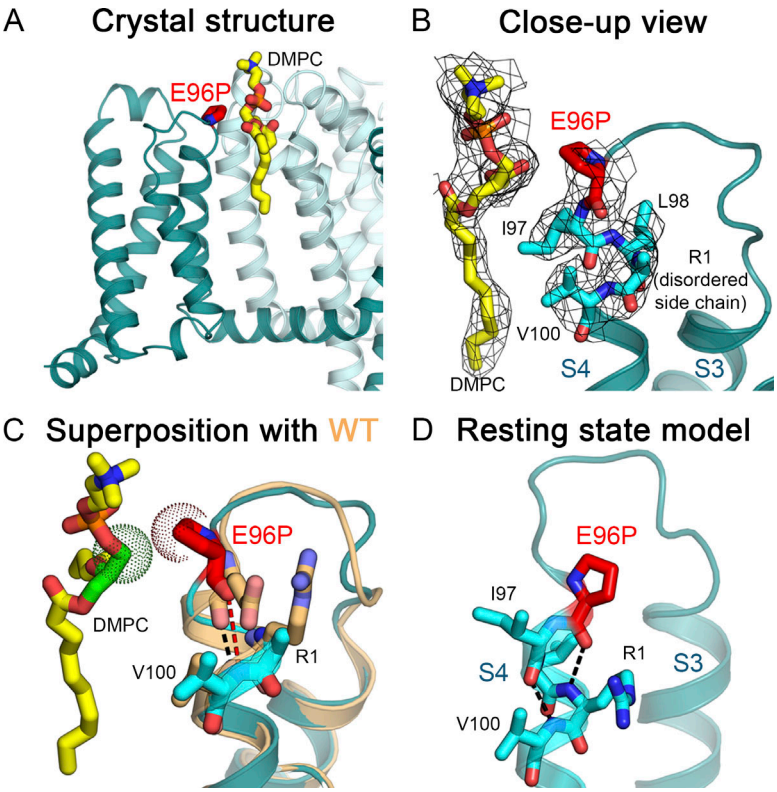

Figure 4. **Structure of Na_VAb/E96P. (A)** Crystal structure of Na_VAb/E96P with the mutation shown in red. **(B)** Close-up view of Na_VAb/E96P structure in the activated state (teal). Residues E96P (red), Ile97, Leu98, Arg99 (**R1**), and Val100 (cyan) are shown as sticks with the σ_A-weighted $2F_O$-F_C electron density map contoured at 1.0σ level overlaid (mesh). A DMPC lipid molecule interacting with E96P is shown as yellow sticks. **(C)** Comparison of Na_VAb/E96P structure (teal) with the structure of Na_VAb WT (light orange). The backbone carbonyl oxygen of Glu96 and the amide nitrogen of Val100 form a hydrogen bond (black dashes) that stabilizes the S4 helix in the WT structure. The E96P mutation breaks the helical conformation of S4 by inducing a longer distance between these atoms (red dashes). The side chain of E96P also interacts with the glycerol backbone (green) of DMPC. The van der Waals hemispheres are shown as dots. Na_VAb/I217C (PDB accession no. 3RVY) was used for the comparison as WT because the S3–S4 loop was not modeled in $Na_VAb\Delta28$ (PDB accession no. 6MWA). **(D)** Homology model of Na_VAb/E96P structure in the resting state. The backbone carbonyl oxygen of E96P and the amide nitrogen of **R1** form a hydrogen bond (black dashes) that stabilizes the 3_{10} helix.

change, the mutation from a charged Glu (or a polar Ser in $Na_V1.7$) to a more hydrophobic cyclic structure (pyrrolidine ring) in Pro likely facilitates amino acid–lipid interactions. Indeed, our structure shows that the Pro side chain ring makes van der Waals interactions with the glycerol backbone of dimyristoylphospatidylcholine (DMPC) from the lipid bicelle used in our preparation (Fig. 4 B). The E96P mutation also causes the gating charge **R1** to become disordered as the electron density for the **R1** side chain is not visible (Fig. 4 B), which may help **R1** to move more freely during the voltage sensor activation. Based on these structural features, the S4 segment is further stabilized in the activated state compared with the WT, most likely by the favorable Pro–lipid interactions.

Mapping of Na_VAb/E96P in the resting state model suggests that protein–lipid interactions contribute to the negative shift of activation. In the resting state model, E96P is part of a 3_{10} helix that includes the entire S4 segment (Fig. 4 D) and points toward the S1 and S2 helices and the aqueous cleft in the same direction as the four Arg gating charges, likely straining E96P in an energetically unstable conformation. Once S4 shifts outward during channel activation, E96P moves outward and unwinds to face the membrane, resulting in increased stabilization of the activated state (Video 2). Thus, a newly formed protein–lipid interaction for E96P in Na_VAb and S211P in $Na_V1.7$, which occurs in the activated state but not in the resting state, likely contributes to the driving force for channel hyperexcitability.

$Na_V1.7$/L823R (Na_VAb/L98R)

Leu at this position is conserved in Na_VAb (Fig. S1) and the first three VSs of $Na_V1.7$ compared with Ile in domain IV. The L98R mutation in Na_VAb produced a −10 mV shift in V_a (Fig. 2 B and Table S2), similar to the −14.6 mV shift for $Na_V1.7$/L823R (Lampert et al., 2009). L98R showed a slower time to peak between −120 and −100 mV compared with Na_VAb WT, but this difference in the activation kinetics disappeared when the membrane potential was in the range of −100 to 0 mV (Fig. 2 C). The mutant also showed a significantly slower inactivation time constant than the WT (Fig. 2 D) in the same fashion as for the L823R mutation in $Na_V1.7$ (Lampert et al., 2009). The backbone conformation in the S4 segment around the mutation from Ile97 to Arg102 (also referred to as **R2**) shifts by as much as 3.6 Å from the conformation in the WT, as measured at Cα atoms (Fig. 5, A–C). In addition, electron density for the L98R side chain as well as the S3–S4 loop is disordered, indicating higher flexibility in this region (Fig. 5 B). Further analysis reveals that the most common side chain rotamers for L98R would clash with the S3–S4 loop seen in the WT, partly explaining why the loop is disordered. The side chain rotamers that can be modeled (red) without a clash displace the first gating charge Arg side chain (R99; also referred to as **R1**) in the WT and point toward the aqueous cleft in parallel with **R1** (Fig. 5 C). The **R2** side chain in the mutant structure also changes conformation to stack underneath the **R1** side chain and it interacts with the extracellular negatively charged residue Glu32 from S1 (Fig. 5 B) instead of making van der Waals interactions with the S3–S4 loop as seen in WT (Fig. 5 C). In the WT structure, Leu98 points its side chain toward the membrane region and the activated state is stabilized by hydrophobic interactions with the lipids (Fig. 5 C). Without a conformational change in the backbone that allows the Arg side chain to point toward the aqueous cleft, the L98R mutation would place a charged side chain in the membrane region and destabilize the channel–lipid interaction. Therefore, the L98R

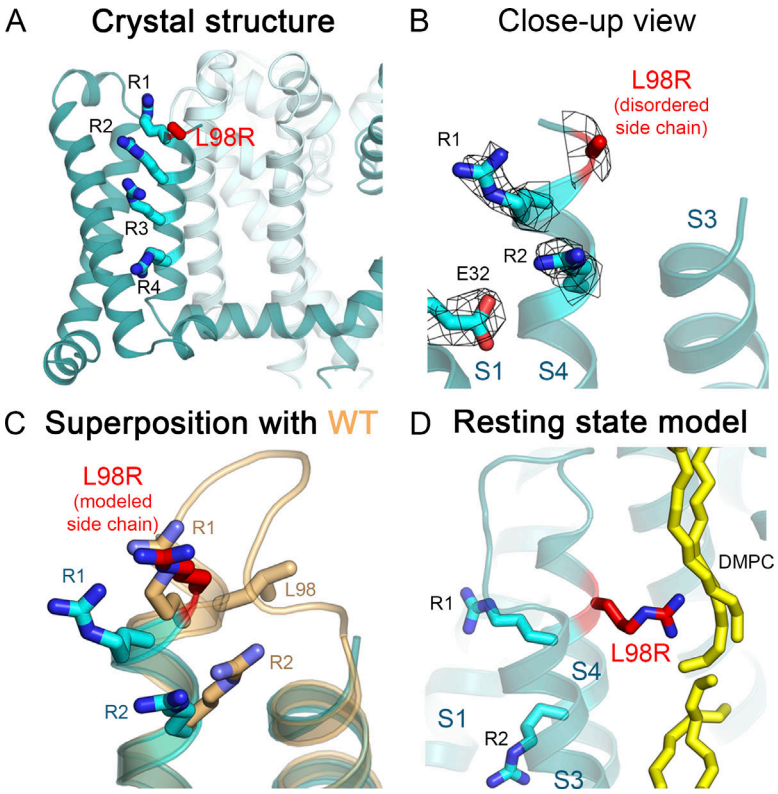

Figure 5. **Structure of Na_VAb/L98R. (A)** Crystal structure of Na_VAb/L98R with the mutation shown in red. **(B)** Close-up view of Na_VAb/L98R structure in the activated state (teal). Side chains of residues L98R (red), Glu32, Arg99 (**R1**), and Arg102 (**R2**; cyan) are shown as sticks with the σ_A-weighted $2F_O$-F_C electron density map contoured at 1.0σ level overlaid (mesh). The S3–S4 loop and the side chain of L98R are disordered. **(C)** Comparison of Na_VAb/L98R structure (teal) with the structure of Na_VAb WT (light orange). A hypothetical model for the L98R side chain (red) is illustrated to indicate a favorable rotamer that does not clash with the S3–S4 loop. Na_VAb/I217C (PDB accession no. 3RVY) was used for the comparison as WT because the S3–S4 loop was not modeled in $Na_VAb\Delta28$ (PDB accession no. 6MWA). **(D)** Homology model of Na_VAb/L98R structure in the resting state. DMPC lipid molecules are shown as yellow sticks to indicate the membrane bilayer.

mutation causes a local conformation change in the S4 segment to overcome this instability by moving the charged Arg side chain from the membrane face toward the polar face of the aqueous cleft (Fig. 5, B and C).

Interestingly, the resting state model of Na_VAb/L98R suggests that the positively charged Arg side chain is buried within the hydrophobic acyl chains of the lipid bilayer (Fig. 5 D). The energy penalty to bury a charged residue in a hydrophobic lipid bilayer likely decreases the stability of the resting state. Since putting the charged side chain of L98R next to the aqueous cleft is much more favorable in the activated state, this mutation may result in a negative shift in V_a due to its unfavorable charge–lipid interactions in the resting state (Video 3).

$Na_V1.7$/F216S (Na_VAb/L101S)

Phe at this position in domains I and II of $Na_V1.7$ is substituted by the similarly hydrophobic residue Leu in domain III and in Na_VAb (Fig. S1). We introduced the F216S mutation into Na_VAb at its equivalent position, Leu101 located next to the second Arg gating charge (Arg102 or **R2**; Fig. S1). Na_VAb/L101S exhibits a −29 mV shift in V_a (Fig. 2 B and Table S2), which is larger than the shift of −11.7 mV observed for $Na_V1.7$/F216S (Choi et al., 2006). We suggest that the large negative shift of V_a comes from the synergistic effects of the mutations in four subunits in Na_VAb in this case. Na_VAb/L101S exhibits a shallower plot for the activation time to peak activation compared with the WT (Fig. 2 C), which recapitulates the biophysical properties of $Na_V1.7$/F216S (Choi et al., 2006). L101S also shows faster inactivation kinetics between −110 and −90 mV but becomes slower in the more physiologically significant voltage range above −90 mV (Fig. 2 D).

The crystal structure of Na_VAb/L101S in the activated state is similar to WT, except for the side chain of L101S, which is smaller and more polar (Fig. 6 A). The L101S side chain points to the lipid region and likely interacts with the acyl chain of the DMPC phospholipid in our lipid bicelle preparation (Fig. 6, A and B). The acyl chain in the phospholipid at this location is well-ordered in the WT Na_VAb structure, but it is disordered by the L101S mutation, indicating high lipid mobility and weak binding due to the polar substitution (Fig. 6 C). In the resting state model of Na_VAb/L101S, L101S is located near the center of the lipid bilayer and likely leads to an even more unfavorable protein–lipid interaction because burying the polar hydroxyl group of Ser deeply in the hydrophobic lipid environment is energetically costly (Fig. 6 D). The resulting destabilization of the resting state may explain the hyperexcitability caused by this mutation (Video 4).

Discussion

IEM mutations are spread broadly through the amino acid sequence of $Na_V1.7$, although they are concentrated mostly in domains I and II (Fig. 1). In previous work, we focused our study on three mutations in the S4–S5 linker that all convert the WT amino acid residue to a Thr and cause sodium channel hyperexcitability by forming a novel hydrogen bond in the activated state between the S4–S5 linker and the pore module (Wisedchaisri et al., 2023). Here, we focused on IEM mutations in the VS of human $Na_V1.7$ where voltage-dependent gating takes place to give new insight into the molecular basis for hyperexcitability in four additional sets of affected IEM families

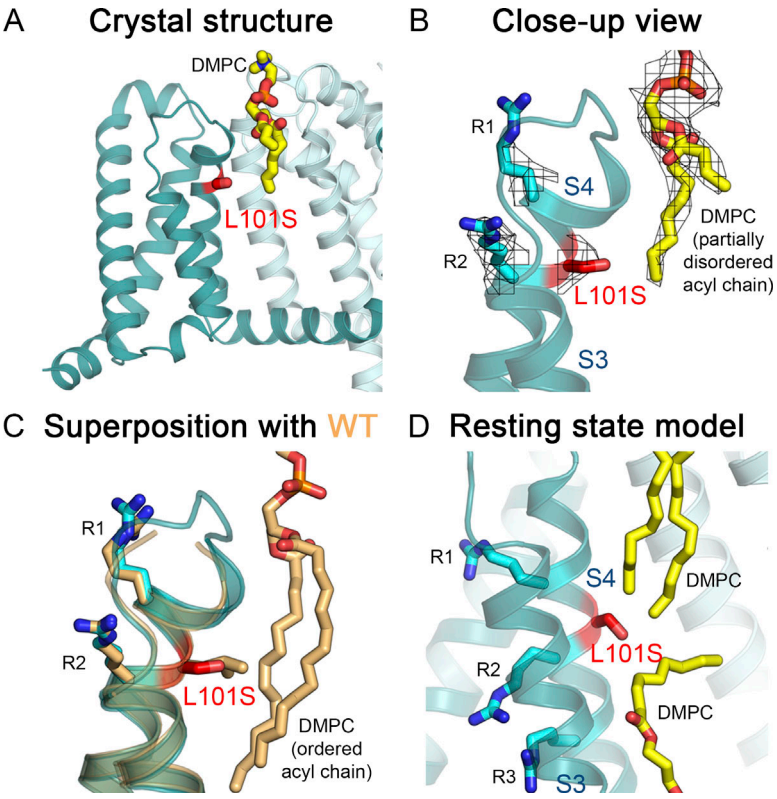

Figure 6. **Structure of Na_VAb/L101S. (A)** Crystal structure of Na_VAb/L101S with the mutation is shown in red. **(B)** Close-up view of Na_VAb/L101S structure in the activated state (teal). Side chains of residues L101S (red), Arg99 (**R1**), and Arg102 (**R2**; cyan) are shown as sticks with the σ_A-weighted $2F_O$-F_C electron density map contoured at 1.0σ level overlaid (mesh). A DMPC lipid molecule potentially interacting with L101S is shown as yellow sticks. The acyl chain of the DMPC is partially disordered. **(C)** Comparison of Na_VAb/L101S structure (teal) with the structure of Na_VAb WT (light orange). The DMPC molecule is fully ordered in the WT structure. $Na_VAb\Delta28$ (PDB accession no. 6MWA) was used for the comparison as WT. **(D)** Homology model of Na_VAb/L101S structure in the resting state. DMPC lipid molecules are shown as yellow sticks to indicate the membrane bilayer. The L101S side chain is buried at the center of the membrane bilayer.

(Table S1). By expressing these selected IEM mutations in the context of the ancestral sodium channel Na_VAb, we were able to crystallize and determine the high-resolution structure of each mutation in its native state with an activated VS. Because Na_VAb structure in the resting state is also known (Wisedchaisri et al., 2019), we were able to use molecular modeling methods to define the effects of IEM mutations on the structures of both resting and activated states. By comparing the structural effects of these mutations in these two states of the VS, similar mechanisms by which these IEM mutants modify VS function became apparent, which define the structural basis for their hyperexcitability.

IEM mutations in the VS modify movements and interactions of the S4 gating charges

Voltage-dependent gating of ion channels depends upon voltage-driven transmembrane movement of the Arg and Lys gating charges in the S4 segments in the VS. In the resting state, the S4 segment is drawn inward by the electrostatic force of the negative membrane potential exerted on its positive gating charges, which interact with the negatively charged residues in the intracellular negative cluster of Glu residues. Upon depolarization, the electrostatic force of the membrane potential is released, the S4 segment moves outward through the hydrophobic constriction site, and the S4 gating charges interact with the extracellular negative cluster of Glu and Asp/Asn residues (Catterall et al., 2017; Wisedchaisri et al., 2019). Our results suggest that IEM mutations in the VS of $Na_V1.7$ (I136V, S211P, F216S, and L823R) facilitate the outward movement of the S4 gating charges by altering their interactions with surrounding amino acid side chains and lipids to stabilize the activated-state and/or destabilize the resting-state conformations.

I136V is located in the S1 segment of $Na_V1.7$-VS1 and forms part of the hydrophobic constriction site that serves as a seal in the VS of domain I. The Ile136 residue is absolutely conserved in all four domains of $Na_V1.7$ and all human Na_V subtypes, underlining the importance of the Ile side chain at this position for normal channel function. Our structural results show that substitution of the shorter side chain of Val136 weakens the interaction with R2 and the hydrophobic constriction site to destabilize the resting state while also creating additional space for the outward movement of the gating charges in the S4 segment of domain I of $Na_V1.7$. The mutation S211P in $Na_V1.7$ causes a local structural change that loosens the helical conformation in the S4 helix and creates a more hydrophobic surface for the S4 helix, where it interacts favorably with a neighboring lipid molecule in the activated VS structure. The mutation L823R introduces an additional positive charge into the S4 segment of VS2 at the position immediately before the first Arg gating charge, and the mutation F216S introduces a hydrophilic residue in the S4 segment of VS1. By burying a charged R823 side chain or a polar Ser216 side chain in the lipid bilayer, these two mutations would greatly destabilize the resting state and thereby negatively shift V_a and promote activation.

All IEM mutations studied here were substituted in Na_VAb, a homotetrameric bacterial sodium channel, instead of the four-domain human $Na_V1.7$ channel. As each mutation is present four times in the homotetramer, this may amplify the effect of the mutation in our electrophysiological characterization. Because each IEM patient possesses only a single IEM mutation, we chose

to characterize these mutations individually. It is possible that all the mutations studied here would have synergistic effects when presented simultaneously. The IEM mutations in the VS of $Na_V1.7$ occur mainly in domains I and II, which have the same number of gating charges as the VS of Na_VAb, making Na_VAb an ideal system to study these mutations. However, Na_VAb may be less appropriate for IEM mutations in domain IV which primarily activates to trigger fast inactivation, and for mutations in $Na_V1.7$ that cause a related condition known as PEPD, which impaired fast inactivation, since Na_VAb lacks an equivalent fast inactivation apparatus found in vertebrate Na_V channels. Na_VAb has a slow inactivation process that causes pore closure, similar to the slow inactivation of eukaryotic Na_V channels (Pavlov et al., 2005). Consistent with previous studies in $Na_V1.7$, most of the IEM mutations studied here in Na_VAb (I22V, L98R, L101S) primarily slowed the rate of inactivation compared with WT in the physiologically important membrane potential range from −100 to −40 mV (Fig. 2 D). On the other hand, E96P showed a slightly faster rate of inactivation (Fig. 2 D), but it is nevertheless consistent with the faster inactivation kinetics for S211P mutation in $Na_V1.7$ (Estacion et al., 2010). It is unclear how the mutations affect the inactivation kinetics based on the structures, as there is no structural change observed in the pore domain. The effects on slow inactivation of IEM mutations expressed in Na_VAb are consistent with their hyperexcitable phenotype in vivo, but they probably do not contribute in a major way to the disease phenotype in most individuals with mutations in human $Na_V1.7$ (Lampert et al., 2014). We note that the E96P mutation in Na_VAb may not fully represent the effect of the S211P mutation in $Na_V1.7$, and the Pro–lipid interaction observed in our structure requires further functional studies in native $Na_V1.7$. Lastly, it will be important in the future to determine experimental structures of $Na_V1.7$ IEM mutants in both the resting and the activated states at high resolution and to conduct molecular dynamics studies in the time scale required for the full functional operation of the channel to further validate these findings.

Conclusion

Our structures of IEM mutants expressed in Na_VAb reveal the structural bases for the pathogenic actions of IEM mutations in the VS of $Na_V1.7$ that cause channel hyperexcitability. In general, these mutations cause little or no change in the backbone of the VS. Instead, our structures indicate that the IEM mutations facilitate the outward movement of the S4 segment by shifting the energetics of the VS by stabilizing the activated and/or destabilizing the resting state, resulting in a negative shift in V_a. This high-resolution information on these focused structural changes gives new insights into IEM pathogenesis at the near-atomic level and provides a molecular template for mutation-specific therapy of this debilitating disease.

Data availability

The data underlying this study are openly available in the Protein Data Bank (PDB) under accession numbers 8DIV, 8DIW, 8DIX, and 8DIY for $Na_VAb\Delta28$ I22V, E96P, L98R, and L101S, respectively.

Acknowledgments

Jeanne M. Nerbonne served as editor.

We thank the beamline staff at the Advanced Light Source for assistance during X-ray data collection and Dr. Jin Li (Department of Pharmacology, University of Washington) for technical and editorial support.

This research was supported by National Institutes of Health research grants R01 NS015751 (W.A. Catterall), R35 NS111573 (W.A. Catterall), and R01 HL112808 (N. Zheng and W.A. Catterall) and by the Howard Hughes Medical Institute (HHMI) (N. Zheng). The Berkeley Center for Structural Biology is supported in part by the HHMI. The Advanced Light Source is a Department of Energy, Office of Science User Facility under Contract No. DE-AC02-05CH11231. This research also used resources from the Advanced Photon Source, a U.S. Department of Energy Office of Science user facility operated by Argonne National Laboratory under Contract No. DE-AC02-06CH11357. The authors acknowledge a research contract with Grünenthal GmbH, which supports drug discovery research related to sodium channels and pain.

Author contributions: G. Wisedchaisri, T.M. Gamal El-Din, N. Zheng, and W.A. Catterall designed research; G. Wisedchaisri, T.M. Gamal El-Din, and N.M. Powell performed the experiments; G. Wisedchaisri, T.M. Gamal El-Din, N. Zheng, and W.A. Catterall analyzed and interpreted the results; G. Wisedchaisri, T.M. Gamal El-Din, N. Zheng, and W.A. Catterall wrote the manuscript; and all authors reviewed and revised the manuscript.

Disclosures: G. Wisedchaisri reported grants from Grünenthal GmbH outside the submitted work. T.M. Gamal El-Din reported grants from Grünenthal GmbH outside the submitted work. No other disclosures were reported.

Submitted: 25 July 2023
Revised: 11 September 2023
Accepted: 10 October 2023

References

Ahern, C.A., J. Payandeh, F. Bosmans, and B. Chanda. 2016. The hitchhiker's guide to the voltage-gated sodium channel galaxy. *J. Gen. Physiol.* 147: 1–24. https://doi.org/10.1085/jgp.201511492

Ahuja, S., S. Mukund, L. Deng, K. Khakh, E. Chang, H. Ho, S. Shriver, C. Young, S. Lin, J.P. Johnson Jr, et al. 2015. Structural basis of Nav1.7 inhibition by an isoform-selective small-molecule antagonist. *Science.* 350:aac5464. https://doi.org/10.1126/science.aac5464

Amarouch, M.Y., and H. Abriel. 2015. Cellular hyper-excitability caused by mutations that alter the activation process of voltage-gated sodium channels. *Front. Physiol.* 6:45. https://doi.org/10.3389/fphys.2015.00045

Catterall, W.A. 2000. From ionic currents to molecular mechanisms: The structure and function of voltage-gated sodium channels. *Neuron.* 26: 13–25. https://doi.org/10.1016/S0896-6273(00)81133-2

Catterall, W.A., G. Wisedchaisri, and N. Zheng. 2017. The chemical basis for electrical signaling. *Nat. Chem. Biol.* 13:455–463. https://doi.org/10.1038/nchembio.2353

Chanda, B., and F. Bezanilla. 2002. Tracking voltage-dependent conformational changes in skeletal muscle sodium channel during activation. *J. Gen. Physiol.* 120:629–645. https://doi.org/10.1085/jgp.20028679

Cheng, X., S.D. Dib-Hajj, L. Tyrrell, and S.G. Waxman. 2008. Mutation I136V alters electrophysiological properties of the $Na_V1.7$ channel in a family

with onset of erythromelalgia in the second decade. *Mol. Pain.* 4:1. https://doi.org/10.1186/1744-8069-4-1

Choi, J.S., S.D. Dib-Hajj, and S.G. Waxman. 2006. Inherited erythermalgia: Limb pain from an S4 charge-neutral Na channelopathy. *Neurology*. 67: 1563–1567. https://doi.org/10.1212/01.wnl.0000231514.33603.1e

Cox, J.J., F. Reimann, A.K. Nicholas, G. Thornton, E. Roberts, K. Springell, G. Karbani, H. Jafri, J. Mannan, Y. Raashid, et al. 2006. An SCN9A channelopathy causes congenital inability to experience pain. *Nature*. 444: 894–898. https://doi.org/10.1038/nature05413

Cummins, T.R., J.R. Howe, and S.G. Waxman. 1998. Slow closed-state inactivation: A novel mechanism underlying ramp currents in cells expressing the hNE/PN1 sodium channel. *J. Neurosci.* 18:9607–9619. https://doi.org/10.1523/JNEUROSCI.18-23-09607.1998

Dib-Hajj, S.D., and S.G. Waxman. 2014. Translational pain research: Lessons from genetics and genomics. *Sci. Transl. Med.* 6:249sr4. https://doi.org/10.1126/scitranslmed.3007017

Dib-Hajj, S.D., and S.G. Waxman. 2019. Sodium channels in human pain disorders: Genetics and Pharmacogenomics. *Annu. Rev. Neurosci.* 42: 87–106. https://doi.org/10.1146/annurev-neuro-070918-050144

Dib-Hajj, S.D., Y. Yang, J.A. Black, and S.G. Waxman. 2013. The $Na_V1.7$ sodium channel: From molecule to man. *Nat. Rev. Neurosci.* 14:49–62. https://doi.org/10.1038/nrn3404

Drenth, J.P., R.H. te Morsche, G. Guillet, A. Taieb, R.L. Kirby, and J.B. Jansen. 2005. SCN9A mutations define primary erythermalgia as a neuropathic disorder of voltage gated sodium channels. *J. Invest. Dermatol.* 124: 1333–1338. https://doi.org/10.1111/j.0022-202X.2005.23737.x

Emsley, P., B. Lohkamp, W.G. Scott, and K. Cowtan. 2010. Features and development of Coot. *Acta Crystallogr. D Biol. Crystallogr.* 66:486–501. https://doi.org/10.1107/S0907444910007493

Estacion, M., J.S. Choi, E.M. Eastman, Z. Lin, Y. Li, L. Tyrrell, Y. Yang, S.D. Dib-Hajj, and S.G. Waxman. 2010. Can robots patch-clamp as well as humans? Characterization of a novel sodium channel mutation. *J. Physiol.* 588:1915–1927. https://doi.org/10.1113/jphysiol.2009.186114

Gamal El-Din, T.M., M.J. Lenaeus, K. Ramanadane, N. Zheng, and W.A. Catterall. 2019. Molecular dissection of multiphase inactivation of the bacterial sodium channel Na_VAb. *J. Gen. Physiol.* 151:174–185. https://doi.org/10.1085/jgp.201711884

Geha, P., Y. Yang, M. Estacion, B.R. Schulman, H. Tokuno, A.V. Apkarian, S.D. Dib-Hajj, and S.G. Waxman. 2016. Pharmacotherapy for pain in a family with inherited erythromelalgia guided by genomic analysis and functional profiling. *JAMA Neurol.* 73:659–667. https://doi.org/10.1001/jamaneurol.2016.0389

Huang, G., D. Liu, W. Wang, Q. Wu, J. Chen, X. Pan, H. Shen, and N. Yan. 2022. High-resolution structures of human Nav1.7 reveal gating modulation through α-π helical transition of S6IV. *Cell Rep.* 39:110735. https://doi.org/10.1016/j.celrep.2022.110735

Klugbauer, N., L. Lacinova, V. Flockerzi, and F. Hofmann. 1995. Structure and functional expression of a new member of the tetrodotoxin-sensitive voltage-activated sodium channel family from human neuroendocrine cells. *EMBO J.* 14:1084–1090. https://doi.org/10.1002/j.1460-2075.1995.tb07091.x

Koishi, R., H. Xu, D. Ren, B. Navarro, B.W. Spiller, Q. Shi, and D.E. Clapham. 2004. A superfamily of voltage-gated sodium channels in bacteria. *J. Biol. Chem.* 279:9532–9538. https://doi.org/10.1074/jbc.M313100200

Lampert, A., S.D. Dib-Hajj, E.M. Eastman, L. Tyrrell, Z. Lin, Y. Yang, and S.G. Waxman. 2009. Erythromelalgia mutation L823R shifts activation and inactivation of threshold sodium channel Nav1.7 to hyperpolarized potentials. *Biochem. Biophys. Res. Commun.* 390:319–324. https://doi.org/10.1016/j.bbrc.2009.09.121

Lampert, A., M. Eberhardt, and S.G. Waxman. 2014. Altered sodium channel gating as molecular basis for pain: Contribution of activation, inactivation, and resurgent currents. *Handb. Exp. Pharmacol.* 221:91–110. https://doi.org/10.1007/978-3-642-41588-3_5

Lee, M.J., H.S. Yu, S.T. Hsieh, D.A. Stephenson, C.J. Lu, and C.C. Yang. 2007. Characterization of a familial case with primary erythromelalgia from Taiwan. *J. Neurol.* 254:210–214. https://doi.org/10.1007/s00415-006-0328-3

Liebschner, D., P.V. Afonine, M.L. Baker, G. Bunkóczi, V.B. Chen, T.I. Croll, B. Hintze, L.W. Hung, S. Jain, A.J. McCoy, et al. 2019. Macromolecular structure determination using X-rays, neutrons and electrons: Recent developments in Phenix. *Acta Crystallogr. D Struct. Biol.* 75:861–877. https://doi.org/10.1107/S2059798319011471

Mantegazza, M., S. Cestèle, and W.A. Catterall. 2021. Sodium channelopathies of skeletal muscle and brain. *Physiol. Rev.* 101:1633–1689. https://doi.org/10.1152/physrev.00025.2020

McCoy, A.J., R.W. Grosse-Kunstleve, P.D. Adams, M.D. Winn, L.C. Storoni, and R.J. Read. 2007. Phaser crystallographic software. *J. Appl. Cryst.* 40: 658–674. https://doi.org/10.1107/S0021889807021206

Murshudov, G.N., P. Skubák, A.A. Lebedev, N.S. Pannu, R.A. Steiner, R.A. Nicholls, M.D. Winn, F. Long, and A.A. Vagin. 2011. REFMAC5 for the refinement of macromolecular crystal structures. *Acta Crystallogr. D Biol. Crystallogr.* 67:355–367. https://doi.org/10.1107/S0907444911001314

Otwinowski, Z., and W. Minor. 1997. Processing of X-ray diffraction data collected in oscillation mode. *Methods Enzymol.* 276:307–326. https://doi.org/10.1016/S0076-6879(97)76066-X

Paavonen, K.J., H. Swan, K. Piippo, L. Hokkanen, P. Laitinen, M. Viitasalo, L. Toivonen, and K. Kontula. 2001. Response of the QT interval to mental and physical stress in types LQT1 and LQT2 of the long QT syndrome. *Heart.* 86:39–44. https://doi.org/10.1136/heart.86.1.39

Pavlov, E., C. Bladen, R. Winkfein, C. Diao, P. Dhaliwal, and R.J. French. 2005. The pore, not cytoplasmic domains, underlies inactivation in a prokaryotic sodium channel. *Biophys. J.* 89:232–242. https://doi.org/10.1529/biophysj.104.056994

Payandeh, J., T. Scheuer, N. Zheng, and W.A. Catterall. 2011. The crystal structure of a voltage-gated sodium channel. *Nature*. 475:353–358. https://doi.org/10.1038/nature10238

Petitprez, S., L. Tiab, L. Chen, L. Kappeler, K.M. Rösler, D. Schorderet, H. Abriel, and J.M. Burgunder. 2008. A novel dominant mutation of the Nav1.4 alpha-subunit domain I leading to sodium channel myotonia. *Neurology*. 71:1669–1675. https://doi.org/10.1212/01.wnl.0000335168.86248.55

Shen, H., D. Liu, K. Wu, J. Lei, and N. Yan. 2019. Structures of human Nav1.7 channel in complex with auxiliary subunits and animal toxins. *Science*. 363:1303–1308. https://doi.org/10.1126/science.aaw2493

Shen, H., N. Yan, and X. Pan. 2021. Structural determination of human Nav1.4 and Nav1.7 using single particle cryo-electron microscopy. *Methods Enzymol.* 653:103–120. https://doi.org/10.1016/bs.mie.2021.03.010

Swan, H., M.Y. Amarouch, J. Leinonen, A. Marjamaa, J.P. Kucera, P.J. Laitinen-Forsblom, A.M. Lahtinen, A. Palotie, K. Kontula, L. Toivonen, et al. 2014. Gain-of-function mutation of the SCN5A gene causes exercise-induced polymorphic ventricular arrhythmias. *Circ. Cardiovasc. Genet.* 7: 771–781. https://doi.org/10.1161/CIRCGENETICS.114.000703

Takahashi, K., M. Saitoh, H. Hoshino, M. Mimaki, Y. Yokoyama, M. Takamizawa, M. Mizuguchi, Z.M. Lin, Y. Yang, and T. Igarashi. 2007. A case of primary erythermalgia, wintry hypothermia and encephalopathy. *Neuropediatrics*. 38:157–159. https://doi.org/10.1055/s-2007-990265

Waxman, S.G., I.S.J. Merkies, M.M. Gerrits, S.D. Dib-Hajj, G. Lauria, J.J. Cox, J.N. Wood, C.G. Woods, J.P.H. Drenth, and C.G. Faber. 2014. Sodium channel genes in pain-related disorders: Phenotype-genotype associations and recommendations for clinical use. *Lancet Neurol.* 13:1152–1160. https://doi.org/10.1016/S1474-4422(14)70150-4

Webb, B., and A. Sali. 2016. Comparative protein modeling using MODELLER. *Curr. Protoc. Bioinformatics*. 54:5.6.1–5.6.37. https://doi.org/10.1002/cpbi.3

Winn, M.D., C.C. Ballard, K.D. Cowtan, E.J. Dodson, P. Emsley, P.R. Evans, R.M. Keegan, E.B. Krissinel, A.G. Leslie, A. McCoy, et al. 2011. Overview of the CCP4 suite and current developments. *Acta Crystallogr. D Biol. Crystallogr.* 67:235–242. https://doi.org/10.1107/S0907444910045749

Wisedchaisri, G., T.M. Gamal El-Din, N. Zheng, and W.A. Catterall. 2023. Structural basis for severe pain caused by mutations in the S4-S5 linkers of voltage-gated sodium channel $Na_V1.7$. *Proc. Natl. Acad. Sci. USA*. 120:e2219624120. https://doi.org/10.1073/pnas.2219624120

Wisedchaisri, G., L. Tonggu, T.M. Gamal El-Din, E. McCord, N. Zheng, and W.A. Catterall. 2021. Structural basis for high-affinity trapping of the $Na_V1.7$ channel in its resting state by tarantula toxin. *Mol. Cell.* 81: 38–48.e4. https://doi.org/10.1016/j.molcel.2020.10.039

Wisedchaisri, G., L. Tonggu, E. McCord, T.M. Gamal El-Din, L. Wang, N. Zheng, and W.A. Catterall. 2019. Resting-state structure and gating mechanism of a voltage-gated sodium channel. *Cell*. 178:993–1003.e12. https://doi.org/10.1016/j.cell.2019.06.031

Wu, M.T., P.Y. Huang, C.T. Yen, C.C. Chen, and M.J. Lee. 2013. A novel SCN9A mutation responsible for primary erythromelalgia and is resistant to the treatment of sodium channel blockers. *PLoS One*. 8:e55212. https://doi.org/10.1371/journal.pone.0055212

Xu, H., T. Li, A. Rohou, C.P. Arthur, F. Tzakoniati, E. Wong, A. Estevez, C. Kugel, Y. Franke, J. Chen, et al. 2019. Structural basis of Nav1.7 inhibition by a gating-modifier spider toxin. *Cell*. 176:702–715.e14. https://doi.org/10.1016/j.cell.2018.12.018

Supplemental material

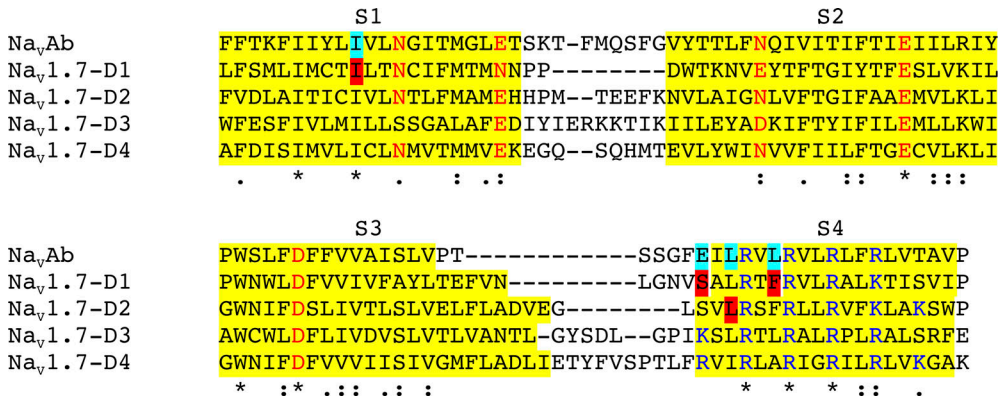

Figure S1. **Multiple amino acid sequence alignments of Na_VAb and human $Na_V1.7$.** Amino acid sequences in the region from S1 to S4 segments are shown. Yellow highlights show the approximate transmembrane boundary. IEM mutations are indicated by red highlight in human $Na_V1.7$ and cyan in Na_VAb.

Video 1. **Predicted transition of Na_VAb/I22V from the resting state to the activated state from the transmembrane view.** I22V, Phe56, and the four Arg gating charges are shown as red, green, and blue sticks, respectively. The S1 and S2 segments are colored in teal, S4 in magenta, the S4–S5 linker in orange, and the pore module S5–S6 in cyan. S3 is omitted for clarity. The morph movie was created based on the resting state homology model and the activated state crystal structure with the transition interpolated based on calculations in PyMol. Playback speed, 30 frames/s.

Video 2. **Predicted transition of Na_VAb/E96P from the resting state to the activated state from the transmembrane view.** E96P and the four Arg gating charges are shown as red and blue sticks, respectively. DMPC lipids are shown as yellow sticks. Dashes indicate distance in Angstrom. The morph movie was created based on the resting state homology model and the activated state crystal structure with the transition interpolated based on calculations in PyMol. Playback speed, 30 frames/s.

Video 3. **Predicted transition of Na_VAb/L98R from the resting state to the activated state from the transmembrane view.** L98R, Glu32, and the four Arg gating charges are shown as red, pink, and blue sticks, respectively. DMPC lipids are shown as yellow sticks. The morph movie was created based on the resting state homology model and the activated state crystal structure with the transition interpolated based on calculations in PyMol. Playback speed, 30 frames/s.

Video 4. **Predicted transition of Na_VAb/L101S from the resting state to the activated state from the transmembrane view.** L101S and the four Arg gating charges are shown as red and blue sticks, respectively. DMPC lipids are shown as yellow sticks. The morph movie was created based on the resting state homology model and the activated state crystal structure with the transition interpolated based on calculations in PyMol. Playback speed, 30 frames/s.

Three tables are provided online. Table S1 lists IEM Mutations. Table S2 shows activation properties of Na_VAb and $Na_V1.7$ with IEM mutations. Table S3 lists X-ray data collection and refinement statistics of $Na_VAb\Delta28$ structures with $Na_V1.7$ IEM mutations in the voltage sensors.